EXPERIMENTAL INVESTIGATION OF FUEL SLOSH IN A GENERIC FIGHTER WING TANK CONFIGURATION

Lisa Debschütz[1], Andreas Seefried[2], Thomas Westermeier[1], Richard Kuchar[2] & David Schwalb[1]

[1]Airbus Defence and Space GmbH, Rechliner Straße, 85077 Manching
[2]German Aerospace Center, Institute of System Dynamics and Control, Münchner Straße 20, 82234 Oberpfaffenhofen-Wessling

Abstract

This paper provides an overview of a joint task between Airbus Defence and Space Manching and the German Aerospace Center (DLR) within the cooperation project framework Diabolo. The performed experimental campaign provides inputs for the following overarching objectives: On the one hand to enable real-time capable fuel slosh modeling methods for in-the-loop flight mechanic simulations of fuel slosh effects and on the other hand to provide a reliable high-fidelity CFD simulation setup for the given application in aircraft tanks pertaining to highly agile aircraft configurations. We describe the motivation of the allover project and specifically the context of the performed ground tests. The selection and construction of the chosen sloshing volume, relevant scaling considerations and used measurement techniques are described in detail. Furthermore, the chosen motion platform is presented, and closely related to the latter, the measurement matrix based on which the experimental campaign was conducted is explained. The processing strategy for the gained data is explained and an outlook is given with respect to the exploitation of the gained data in the further course of the project and future work.

Keywords: Sloshing, Highly Agile Aircraft, Flight Dynamics

1. Introduction

Highly agile aircraft configurations strongly rely on their Flight Control System (FCS) to satisfy safety and performance requirements. Flight control laws are designed to artificially stabilize contemporary, inherently unstable aircraft configurations and at the same time maximize their maneuverability, making the FCS a critical part of the system. To correctly assess the functionality and robustness of the governing control laws during the design and the clearance process, it is crucially important to be able to reproduce the forces and moments acting on the airframe at each point in time. In fighter aircraft flight mechanic clearance, the acting forces and moments are modeled with different degrees of fidelity. Loads originating from fuel slosh are currently implicitly considered using a conservative static fuel position. As a result of this approach for the inclusion of sloshing effects in flight mechanic simulations, the entailed level of tolerance leads to overly pessimistic scenarios for the majority of flight states contemplated in the design and clearance process of the FCS. With fuel fractions continuously increasing on modern, highly agile fighter aircraft, a means to model dynamic sloshing phenomena is gaining further importance. To optimize the aircraft performance, the dynamic effects of fuel sloshing need to be considered in terms of their overall flight mechanic impact as sketched in figure 1.

While the effect of sloshing has been subject to investigation for civil aircraft configurations, including extensive experimental studies (i.e. [1]), much less work has been done in this respect for highly agile configurations. The ongoing Fuel Sloshing project in cooperation between the German Aerospace Center (DLR) and Airbus Defence and Space in Manching primarily aims at providing a real-time capable Reduced Order Model (ROM) method to model dynamic sloshing effects in highly agile aircraft
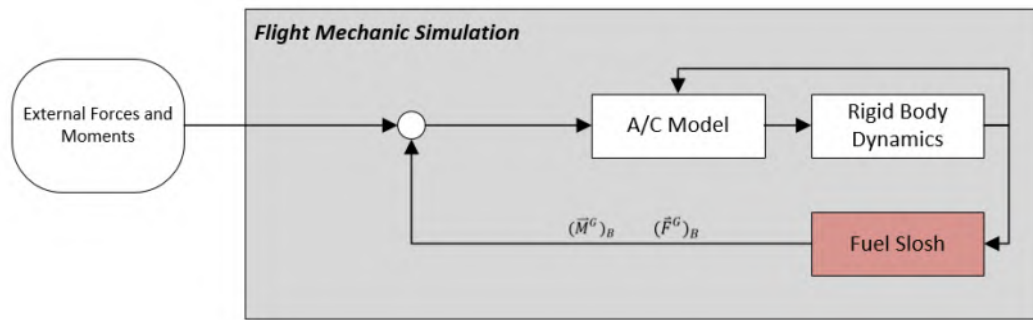
Figure 1 – Impact of dynamic fuel slosh effects on overall flight dynamics.

for the application in the loop with flight mechanic simulations. Mid- and high-fidelity methods are considered in the scope of this project both for the purpose of tuning and validating ROM as well as to provide a reliable simulation tool-chain for detailed treatment of specific cases within the scope of the target application. Experience with traditional Computational Fluid Dynamics (CFD) as well as Smoothed Particle Hydrodynamics (SPH) simulations in this context has shown that the flow problem imposed by typical tank structures within highly agile aircraft configurations in conjunction with operationally relevant use cases is far from trivial and that dedicated ground tests were needed both to validate and optimize simulation setups.

This paper outlines the design, preparation and execution of a ground test which covers the key aspects of the flow phenomena whose macroscopic effects are to be modeled. Obtained results thus serve as a consolidated basis for performing the above-mentioned validation and tuning activities for further use of high fidelity and reduced order modeling methods in the loop with flight mechanic simulations.

The sloshing volume is derived from a typical fighter wing tank topology, being comprised of six connected compartments within a skewed flat shape. The tests were carried out at the Institute of System Dynamics and Control of the German Aerospace Center in Oberpfaffenhofen, which is where the used motion platform is located. The latter is a KUKA KR 500 robot [2]. It provides the benefit of a comparatively large movement range, which was exploited to test both generic trajectories and operationally relevant scenarios with maximum accelerations of up to $2\,\mathrm{g}$.

An iterative process was used in order to find the optimal compromise between covering the most important aspects of the real flow problem occurring in flight and the constraints imposed by the used platform. The representative fighter wing tank subsection along with typical accelerations encountered in flight and Jet A as a fluid characterize the realistic scenario. However kinematic, spatial and loads constraints along with safety considerations had to be taken into account to arrive at a feasible test setup. Scaling considerations in the context of this process aimed at resulting Froude and Reynolds numbers in the order of magnitude of the real scenario to account for comparability of the tested and thus validated scenario with real applications.

Comprehensive video recordings of the fluid movement within the different compartments are provided by eight cameras attached to the ground test structure. Two inertial measurement units mounted on the base plate account for capturing acceleration and angular rate values, while a force-torque sensor placed between the robot and tank flanges records the forces and moments resulting from each tested trajectory. In the framework of CFD and SPH validation activities based on the obtained ground test results, accelerations and angular rates will be fed as an input to the simulation, and forces and moments will be compared to assess the degree of deviation between simulation and experiment.

The measurement matrix comprises both generic maneuvers to cover the fundamental system behavior as well as operationally relevant trajectories. Additionally, varying fill levels as well as different topologies for the connecting holes between tank compartments were tested.

2. Selection of base geometry

In the context of the approach to aim for high-, mid- and low-fidelity methods, the ground test was set up to produce a data pool which will allow the validation of the high- and mid-fidelity methods. These will then, once validated, provide reliable data for tuning real-time capable ROM.

The sloshing volume for the ground test thus has to be chosen carefully. It must represent important geometric characteristics that contribute to shaping the flow problems which are decisive in the given application, but on the other hand must be generic enough in order to provide a database suitable for validation activities. In the context of its validation purpose, the chosen geometry shall feature possible variations and increments in complexity that enable tracing a mismatch between simulation and experimental results back to the representation of a certain feature. Furthermore, the chosen geometry shall specifically include characteristics that have already proven difficult to model using high- and mid-fidelity methods. This is the case for the flow through the compartments, for instance. With roll rates in the range of $250\,\mathrm{deg/s}$, lateral slosh and particularly slosh in conjunction with cross-flow through compartment connectors due to the high resulting centrifugal forces is an essential feature to be mirrored in the chosen experimental geometry.

To account for the basic dominant characteristics of the geometry, the fundamental topology of the flow volume is oriented towards the subsection of a structure as would be typically found in the wing tank of a highly agile aircraft configuration, see also figure 2. The allover shape is a flat, skewed hexahedron that is divided into several subsections. Each of them has a rather elongated shape, and the longest edge exceeds the height by approximately one order of magnitude (with height denominating a direction pointing more or less in the z-axis direction of the body-fixed coordinate system of an aircraft as visible in figure 2b). The separating walls between the six compartments incorporate connector holes as visible schematically in figure 2b. While one possible topology of those connector holes is depicted here, the separator walls were designed interchangeable. Variations in this respect are addressed further in the scope of the measurement matrix description.

The number of compartments was chosen such that on the one hand requirements in terms of limiting mass and size imposed by the used motion platform could be respected while at the same time preserving a configuration where cross-flow between differently sized compartments can take place. The latter is presumed to be one vital driver for the observed flow topologies shaping the resulting time-history of the macroscopic sloshing effects that are of interest for the regarded application. The six compartment configuration provides the opportunity to monitor several in- and outflow compositions, featuring the middle compartments with connector holes on three sides. In compliance with realistic wing tank geometries, care was taken for the connected compartments to be of significantly different size. This was considered important to capture the behavior that results from the fact that the connected compartments differ significantly with respect to their own eigenfrequencies.

While real internal wing tank structures of course comprise a lot more constructive elements in their interior, it was decided to stick to the level of detail shown in figure 2b, basically broken down to a clean flow volume to start the validation activities with an acceptable level of complexity. The influence of geometric details inside the tank on the macroscopic sloshing effects may be subject to future investigations.

Scaling considerations and the entailed final tank dimensions are addressed further on in this paper.
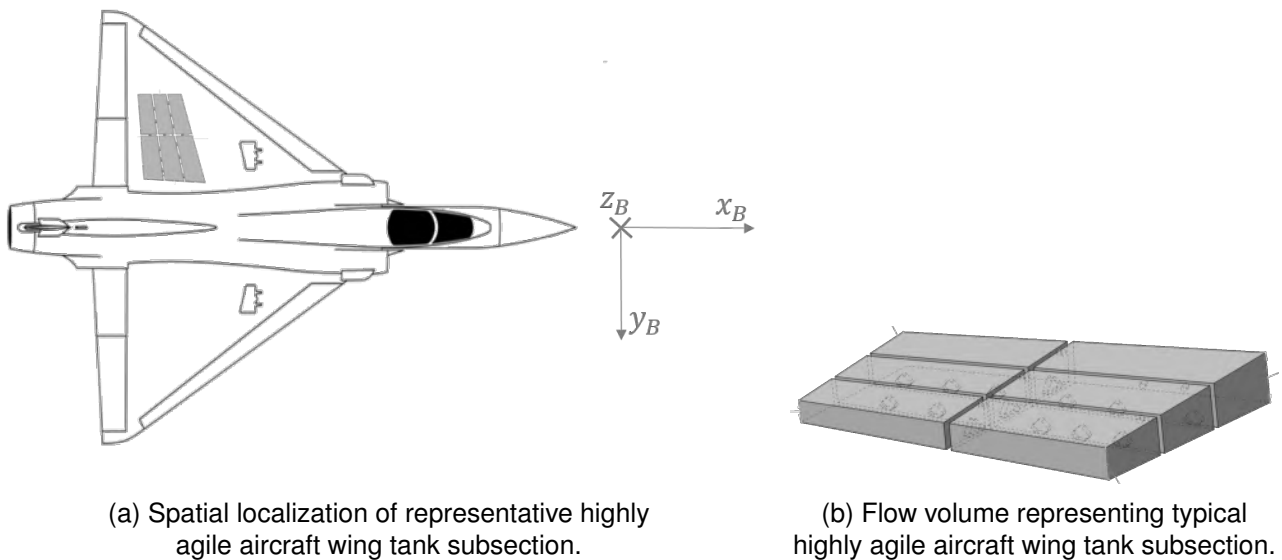
(a) Spatial localization of representative highly agile aircraft wing tank subsection.

(b) Flow volume representing typical highly agile aircraft wing tank subsection.

Figure 2 – Base geometry derived from typical aircraft wing tank.

3. Robotic Motion Platform

An industrial robot is utilized for the generation of stimulation motions for fluid sloshing. The KUKA KR 500 can carry up to $500\,\mathrm{kg}$ in a workspace of around $68\,\mathrm{m}^3$ with its six axes. In addition to that, the robot is mounted on a $8\,\mathrm{m}$ linear rail, greatly extending the workspace and providing more flexibility for different tasks. Usually the robot is used as a full motion simulator and is also known as the "DLR Robotic Motion Simulator" [2]. At the flange of the robot, the tank with its test bed including devices for measurement and illumination as described further on in this paper is mounted.

The movement of the robot is commanded over an interface defined by the manufacturer called "Robot Sensor Interface". Here, every $12\,\mathrm{ms}$ a new set of commands for all seven axes is generated by the path-planning algorithm. This is done with specifically created models based on the DLR Robots library [3]. With this approach, it is possible to create point-to-point (PTP) movements in joint space, to perform path-planning in Cartesian space and to use online methods for inverse kinematics calculations which compute the required joint angles. The provided algorithms consider the limits of the robot, namely the minimum and maximum joint angles, joint angle velocities and joint angle accelerations.

For the usage in this application, not only the maximum acceleration level, but also the gradient of the acceleration is of special interest. Because of the serial composition of the robot, it is not easy to deduce a general statement about a maximum acceleration gradient in the entire workspace. The maximum possible acceleration and jerk are highly dependent on the current joint angle configuration and the desired direction of the movement. However, the manufacturer states that it is possible to obtain a maximum acceleration of around $2\,\mathrm{g}$.

In figures 3a and 3b, the total workspace of the robot is shown at a fixed position on the rail for two different orientations of the robot flange. Here, the flange points 'forward' in the $+x$ direction and the pitch angle is $0°$ in figure 3a and $-32°$ in figure 3b.

To analyze the possible accelerations which the robot can fulfil, figure 4 shows the x-z-Layer of the configuration shown in figure 3a with a pitch angle of $0°$. The color-bar indicates the maximum possible acceleration in the body-fixed $+x$-direction in figure 4a and in $-z$-direction in figure 4b depending on the position of the flange at the beginning of the movement. In this configuration, the body-fixed coordinate system is identical to the inertial system.

One of the boundary conditions imposed by the robot on the tank design is related to the maximum payload and the position of the center of gravity (CoG) of the tank. Figure 5 shows the maximum payload depending on the position of the CoG that is decreasing with the distance to the flange because of the increasing torque.

4

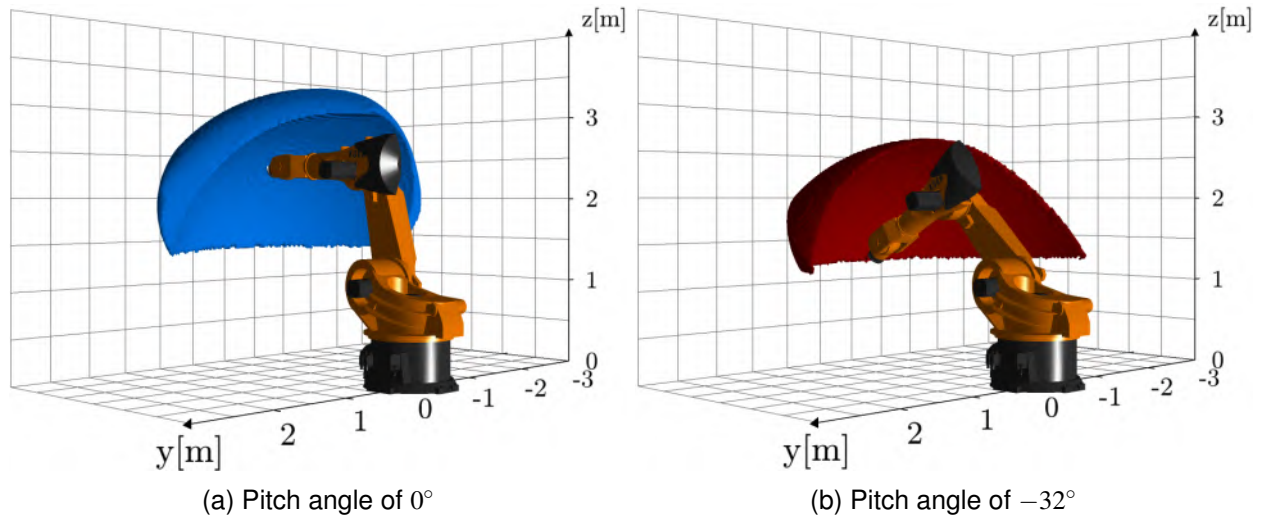(a) Pitch angle of $0°$ (b) Pitch angle of $-32°$

Figure 3 – Possible positions of the robot flange for a fixed orientation considering all joint limits of the system. Reprinted from [5] with permission.
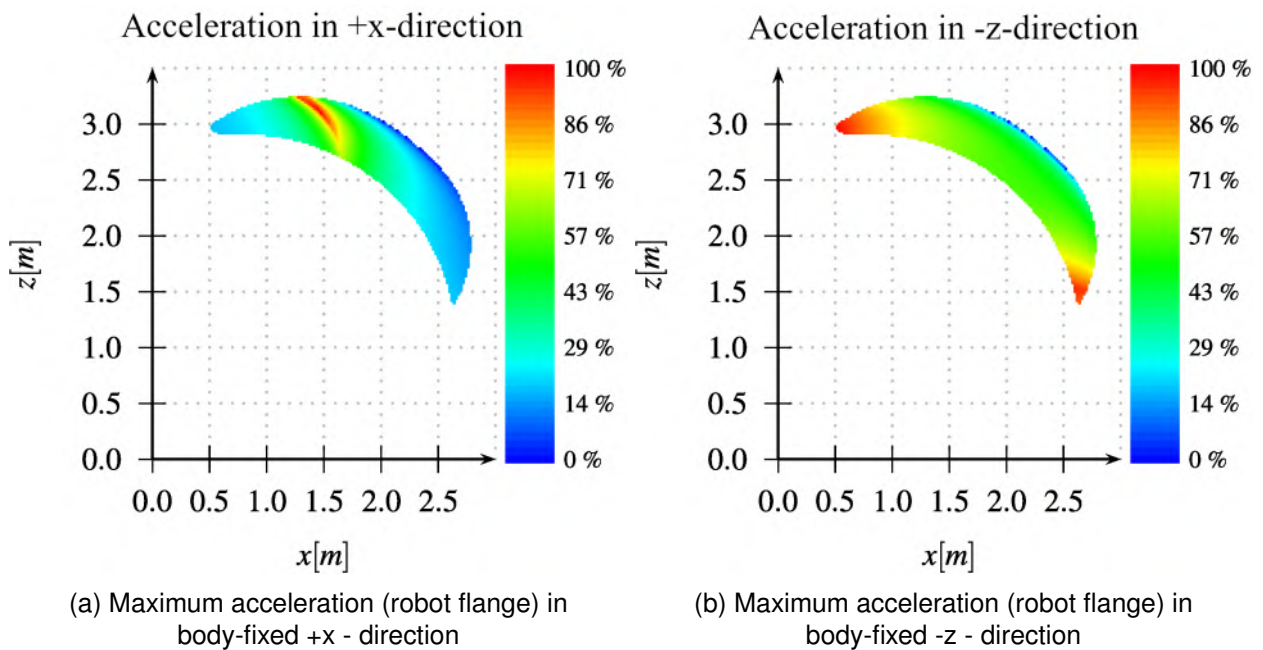

(a) Maximum acceleration (robot flange) in body-fixed +x - direction   (b) Maximum acceleration (robot flange) in body-fixed -z - direction

Figure 4 – Possible accelerations of the robot flange with a fixed orientation in different directions. Reprinted from [5] with permission.
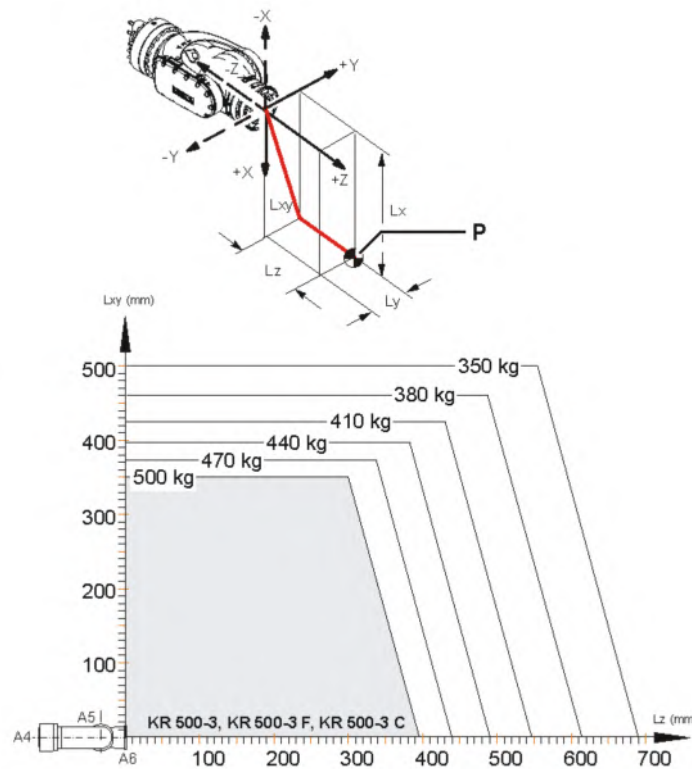
Figure 5 – Maximum payload on the robot depending on the distance of the CoG to the flange.
Figure taken from [4, p. 29]

4. Experimental Setup

4.1 Iterative Design Process

The selection of the motion platform and basic geometric shape form the baseline of the final experimental configuration. In an iterative process, a compromise had to be found between the real scenario and the boundary conditions imposed by the experimental framework in order to find a feasible setup which at the same time represents the flow phenomena for which a validation of mid- and high-fidelity methods is sought. Figure 6 shows a schematic of the iterative process and the boundary conditions considered.

The real scenario in terms of the size of the aforementioned six compartment tank, the acceleration levels that the aircraft internal tank experiences through carefree maneuvering of a highly agile configuration, and the fluid that produces the sloshing cannot be reproduced 1:1 in the planned ground test. A number of boundary conditions are imposed by the used motion platform and experimental site. The constraint layer depicted in figure 6 must be checked against in each iteration of the tank and experiment design loop.

Kinematic constraints refer to the feasibility of desired trajectories on the chosen motion platform. Despite the large workspace of KUKA KR 500, the same characteristics as in flight in terms of maximum accelerations cannot be reached. As far as loads constraints are concerned, care must be taken not to exceed the maximum rigid body mass depending on the location of the test bed CoG relative to the tool center point (see also figure 5). A conservative estimation of the expected sloshing effects was done to avoid emergency stops in test. Spatial constraints refer to the fact that an excessively large platform could lead to parts of the workspace not being usable due to possible collisions between the test bed and the motion platform. Safety constraints limit the scope of fluids that come into question for usage at the experimental site. Any flammable substances or fluids that otherwise present a risk to the ground test crew in the case of a leakage cannot be used.
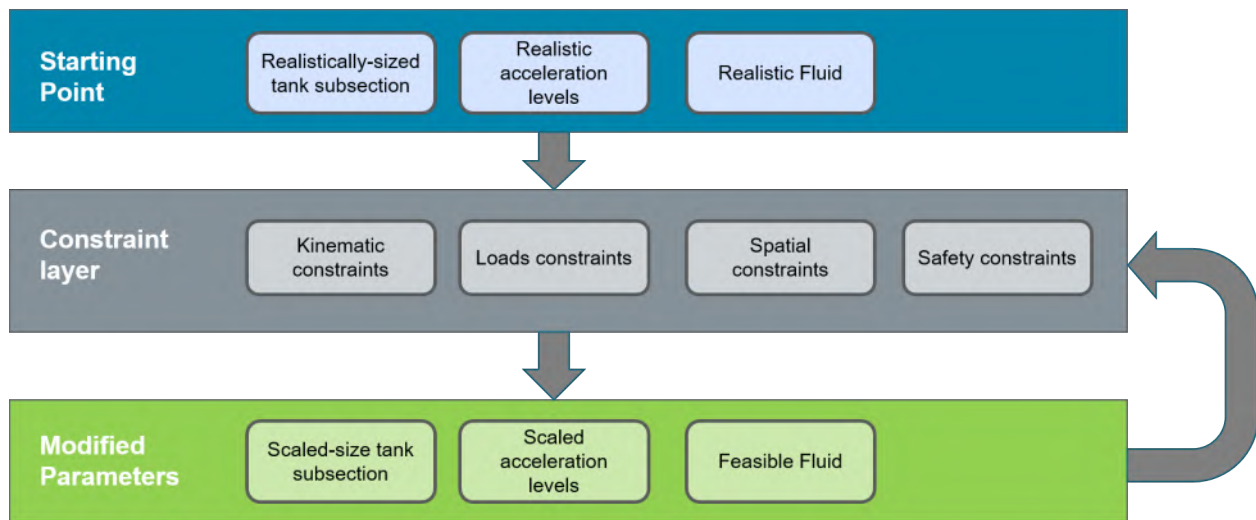
Figure 6 – Iterative test bed design process.

On top of complying with the boundary layer constraints, the final platform design must fulfil additional requirements related to the validation purpose, primarily the inclusion of necessary measurement equipment for reproduction of the trajectory in simulation as well as comparison with the resulting mid- and high-fidelity modeling results. As mentioned, a certain degree of modularity is desired on top of this, providing the possibility to use different internal separating walls inside the tank.

The parameters which are subject to variation for the experimental setup are strongly interconnected, but have to comply with both the given constraints and the targeted test requirements at the same time. As a result of the iterative process, the scaling factor for the tank volume geometry, the down-scaling of the original accelerations and maneuvers towards feasible trajectories, the selection of an alternative fluid and the detail construction of the entire test bed are derived.

4.2 Scaling considerations

Despite the experimental setup having to be compliant with a number of boundary conditions, it is crucially important to nevertheless cover the substantial fluid dynamic properties of the original scenario. Even though data gained in the experiment is not scaled back and applied in the context of the original, but compared to simulation data that is based on the model geometry, mechanical similarity must still be fulfilled between the extreme cases encountered in terms of exerted accelerations in the original and associated scenarios covered in the model. Otherwise, the CFD validation would not factor in the whole scope of the aimed at application.

For transferability between model and original, mechanical similarity must be given. According to [14], three criteria must be met to this end:

1. Geometric similarity

2. Kinematic similarity

3. Dynamic similarity

A dedicated study was conducted in the preparation phase to investigate scaling effects as well as possible setup alterations for compliance with the above given criteria for mechanical similarity [15]. At the focus of these considerations were the Froude (Fr) and Reynolds (Re) number ratios. These fluid dynamic key figures are defined in equations 1 and 2:

$$\mathrm{Fr} = \frac{u}{\sqrt{gL}} \tag{1}$$

$$\mathrm{Re} = \frac{uL}{\nu} = \frac{\rho u L}{\mu} \tag{2}$$

Here, ρ is the density of the fluid $(\mathrm{kg\,m^{-3}})$, g is the gravitational constant $(\mathrm{m\,s^{-2}})$, u is the flow speed of the fluid $(\mathrm{m\,s^{-1}})$, L is a characteristic linear dimension (m), μ is the dynamic viscosity of the fluid $(\mathrm{Pa\,s})$ and v is the kinematic viscosity of the fluid $(\mathrm{m^2\,s^{-1}})$. The Froude number is a measure for the ratio of the flow inertia to the external field (gravitational field), while the Reynolds number is a measure for the ratio of inertial forces to viscous forces.

As evident from the key figure definitions, Froude and Reynolds ratios can be influenced by the geometric scaling factor, the velocity of the fluid (which is implicitly defined by externally applied accelerations) and the fluid properties used in test. These aspects were contemplated in the context of the aforementioned study [15].

In the final configuration, the geometric subsection is not scaled as compared to a realistic wing-tank subsection size. Up-scaling the tank volume would have further improved the Reynolds and Froude ratios, however the trade-off with entailed increased weight and reduced kinematic operational space for collision avoidance would not have been satisfying. Using water as a fluid in test, and despite the significant scaling factor in terms of reached maximum accelerations and acceleration gradients in test compared to extreme realistic scenarios, Froude and Reynolds number could be shown to be in the same order of magnitude in the final model and original scenario.

4.3 Test bed

The core of the test bed resulting from the iterative process is the tank volume enclosed by Macrolon plates. The latter features dimensions as shown in figure 7, resulting in a total volume of approximately $170\,\mathrm{L}$. The Macrolon housing is a screwed construction making use of brass inserts to enable repeated disassemblies with more ease and without damaging the Macrolon irreversibly. The latter is especially important to enable a repeated removal of the tank top, which is necessary for changing the separator walls. Since one of the requirements of the test bed is modularity w.r.t the latter, their fixation is designed for a separator wall change to be feasible while the test bed is mounted on the motion platform. A plug system is used along with screwed connections between the separator walls and the tank outer walls, including the aforementioned brass inserts.
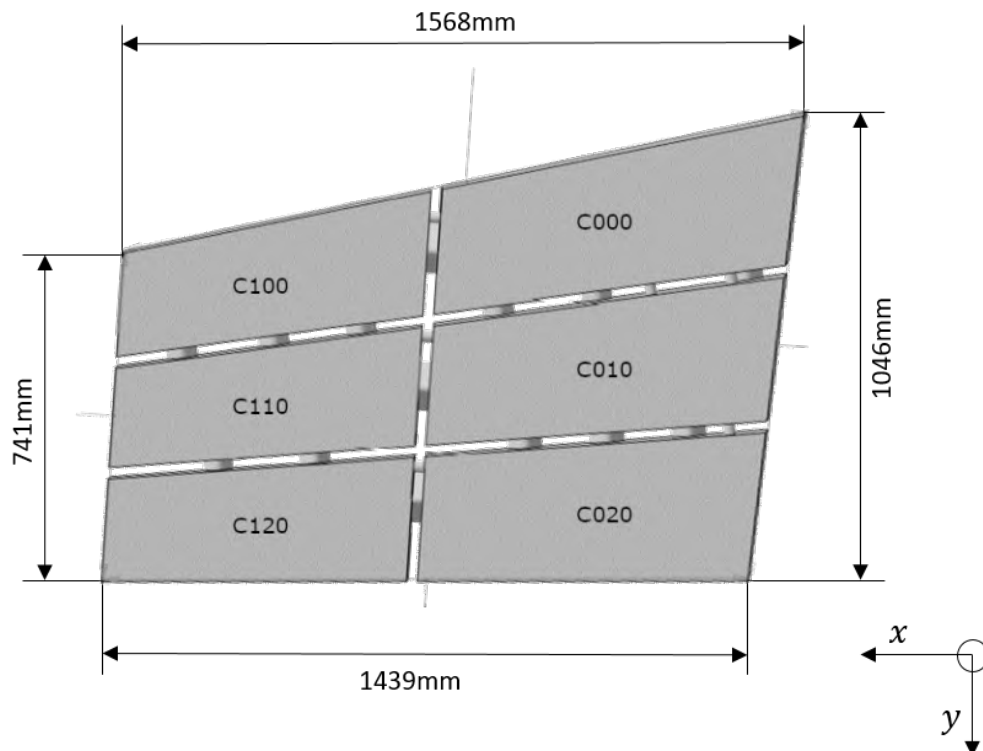

Figure 7 – Tank volume dimensions and cell designation.

Figure 8 shows the Macrolon housing during the building process, illustrating one of the three used sets of separator walls. The tank is sealed making use of sealing chords located at each Macrolon plate joint.
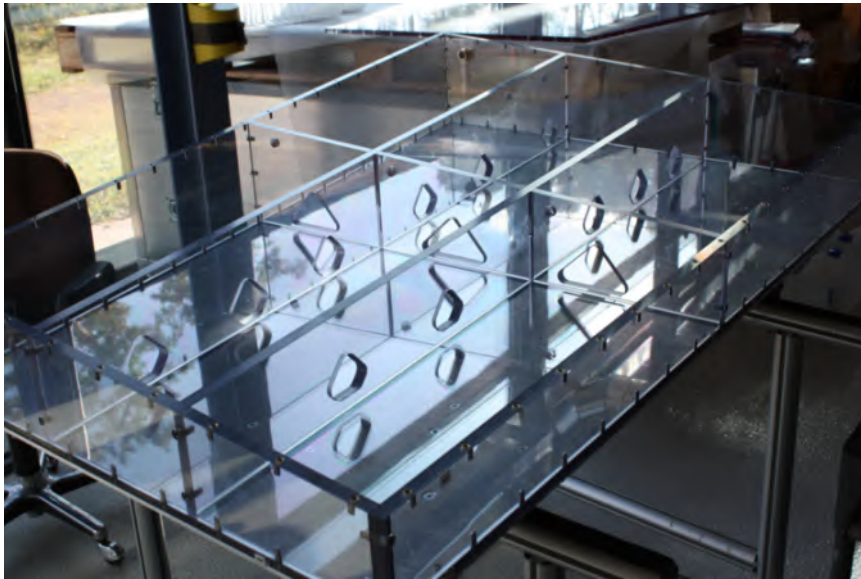

Figure 8 – Macrolon housing during construction.

The Macrolon housing is mounted on a $5\,\mathrm{mm}$ Aluminum base plate. The latter is reinforced by four rectangle profiles as shown in figure 9b. All rectangle profiles are welded to a cylindrical connector. A flange plate is partly screwed, partly welded to that same connector. This welded flange plate is screwed to another adapter plate that hosts the force-torque sensor from the tank-side, as can be seen in figure 9b.

Carbon fibre tubes are attached all around the tank to hold the Aluminum housings for each of the eight cameras surrounding the tank and monitoring the sloshing movements inside the individual compartments. Their attachment to the tank is designed in such a way to allow the necessary degree of freedom for detail orientation in the calibration phase of the ground test while at the same time providing a very stable positioning of each camera when fastened. Aluminum bars each holding a number of LED are attached on top of each camera housing for lightning of the fluid, as can be seen in figure 9c. An additional adapter plate between force-torque (FT) sensor and Robot flange accounts for the connection to the robot.

For the design of the test bed, the significant load case is the emergency stop of the robot, during which up to $5\,\mathrm{g}$ can be reached as opposed to regular operation, where only up to $2\,\mathrm{g}$ are attained. While for the first design loop, an analytical estimation based on plate theory was done for the thickness of the Macrolon plates based on this scenario (see also [15] for the estimation of the pressures acting on the tank walls), later on a dedicated stress analysis was performed for the case of the emergency stop. For this purpose, step accelerations of $5\,\mathrm{g}$ were contemplated along two axes directions for the maximum encountered fill level used in test. CFD calculations provided the resulting dynamic response in terms of forces and moments acting on the tank in a suchlike scenario. The dynamic overshoots over the quasi-static response are thereby derived. In the stress analysis, the hydrostatic pressure distribution of the maximum acceleration to be expected in the emergency scenario, multiplied with the derived overshoot factor, is contemplated. To be conservative, a fill level exceeding the maximum one used in test by $8\,\%$ is taken into account for the stress analysis. Most critical points of the design are the screws holding the tank top, however compliance is achieved with the emergency stop load case.

Figure 9 features both the top and bottom view of the experimental platform that is attached to the motion platform.
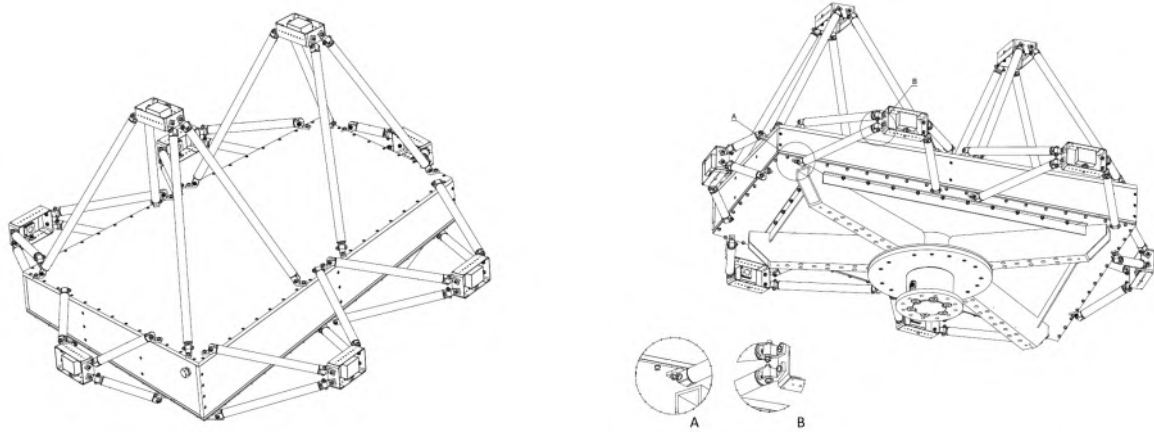
(a) Schematic top view of the test bed.

(b) Schematic bottom view of the test bed.
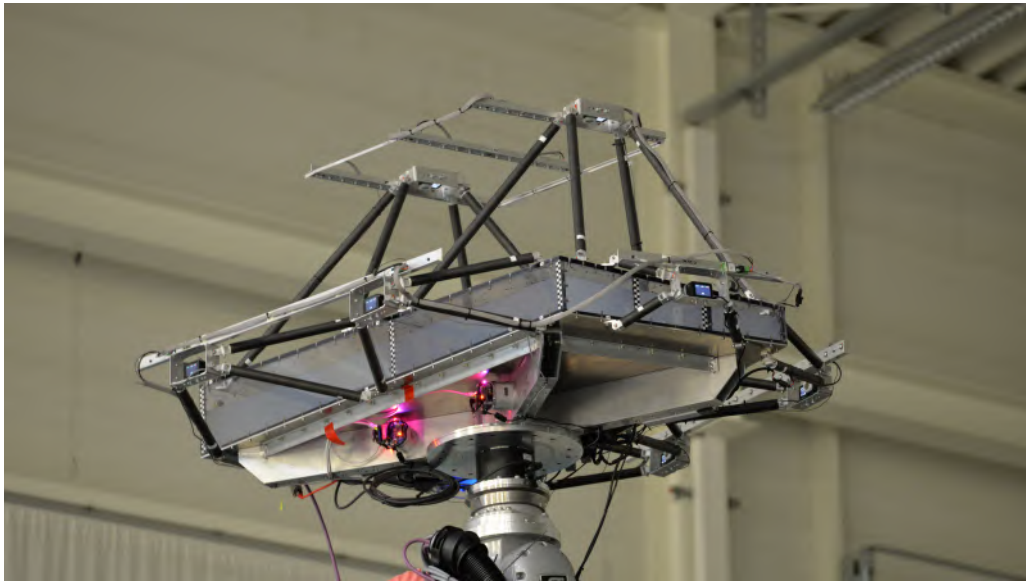
(c) Mounted test bed.

Figure 9 – Test bed as used in the experiment.

4.4 Instrumentation

Sufficient instrumentation must be included on the test bed to be able to reproduce the trajectories driven in test as accurately as possible as well as to track the resulting macroscopic fuel slosh effects for comparison with the simulation results in the framework of the aimed at validation activities.

As sketched in figure 10, two Litef yIMU-IC inertial measurement units (IMU) were used in order to record the accelerations and angular rates performed by the robot. This is necessary despite the target trajectories being nominally known a priori since the response of the robot controller is not 100% predictable in the context of the robot itself and the structure attached to the tool center point not being fully rigid, but featuring unknown dynamic responses due to the sloshing. Deviations from prescribed trajectories are thereby captured for the accurate trajectory to be provided for recalculations. The used IMUs feature a sample rate of $1\,\text{kHz}$ and can capture occurring accelerations with a bias repeatability of $\leq 3\,\text{mg}$. More information about the sensors can be found in [7]. The two IMUs are placed on the reinforcement profiles of the Aluminum base plate of the test platform, as can be seen in figure 12.

To capture the resulting forces and moments, a FT sensor is additionally used to record the macroscopic effects of the resulting slosh. Forces and torques are captured through the K6D175 sensor by ME-Meßsysteme. A sample rate of $1\,\text{kHz}$ is used in test. The sensor provides an accuracy class of $0.5\,\%$. It is placed between the robot flange and tank platform flange, making use of dedicated
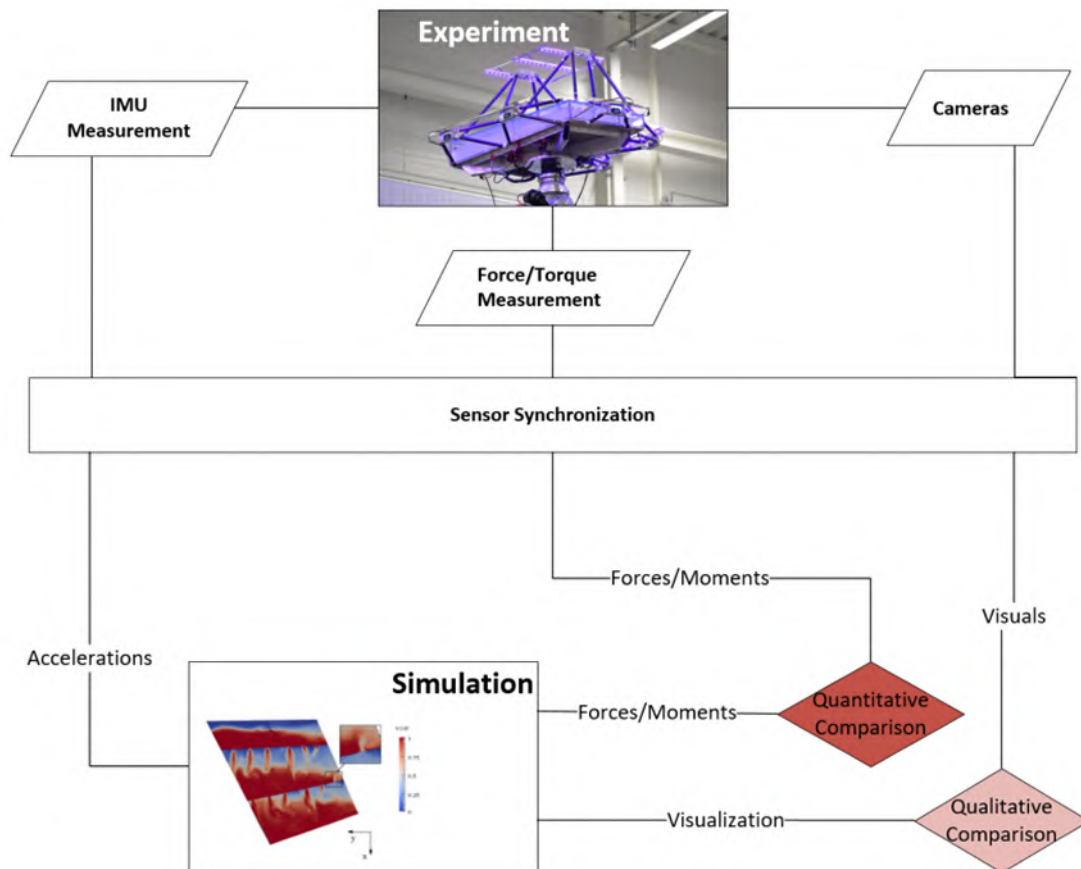
Figure 10 – Sensors

adapter plates to match the respective bolt plates. The resulting forces and torques are the primary source of comparison for the planned validation activities. For the selection of the FT-sensor, care has to be taken to cover the maximum possibly encountered loads. For the sensor selection, the limiting scenario is again the robot emergency stop reaching up to $5\,\mathrm{g}$. An overshoot factor over the associated rigid body loads due to the sloshing was derived from preliminary CFD simulations analogous to the contemplation done for the static proof described above.

For an additional qualitative visual impression of the events inside the tank, eight cameras and accompanying light bars are positioned around the tank to gather video footage during the tests. Consumer grade GoPro HERO9 Black have been chosen because they are lightweight, self-contained and cost-efficient. In the final configuration, a sample rate of 240fps along with a resolution of 1080p is used in "Linear" mode (to preserve a undistorted image). Hyper-smoothing is not used in order to obtain the largest possible angle of sight and therefore be able to reduce the distance of the camera from the tank platform. Different fluid configurations (including or excluding Fluorescein as an additive) are investigated along with different camera settings. In the final configuration, including the Fluorescein additive resulted in the best option. White balance and ISO settings of the used cameras are optimized for this configuration to be set to automatic / 1600 respectively. The LED wavelength ($400\,\mathrm{nm}$) is chosen to stimulate the fluid containing Fluorescein. The wavelength of the light emitted by the Fluorescein is significantly larger than $400\,\mathrm{nm}$, which is why edge filters are placed in front of every camera lens to filter the $400\,\mathrm{nm}$ LED light from opposite tank sides, potentially impairing the resulting image, while the fluid motion is still perfectly visible. Checkerboard tape is attached on the tank walls where the internal walls connect to the outside walls for quantification of the fluid levels inside the tank in the GoPro recordings.

An interface was created to select the upcoming experiment in each execution iteration. A global input signal triggers the robot, the sensors and the illumination to start as well as to stop. As far as

the cameras and the lighting circuit are concerned, the control is achieved by a Raspberry Pi4 single board computer that is also mounted on the underside of the tank assembly. It receives the start and stop signal from the robot control program using TCP/IP and forwards the signal to the cameras using a Bluetooth connection. At the same time, it provides a digital output signal to switch on the lighting circuits while the test is running. The main problems encountered are the cameras overheating after prolonged use which leads to inconsistent Bluetooth connections and crashes in the camera's software. A local NTP server is provided to synchronize the internal clocks of the different devices. Prior to the actual experiments, the delays between the systems have been identified to be less then $5\,\mathrm{ms}$ so that the received data can be taken as synchronized for the evaluation of the experiments. However in the case of the cameras, the startup delay after having received the global signal is significant. Therefore, while the start of illumination visible in the videos can unambiguously be associated with a precise point in time through the used NTP snapshot, a manually generated sound signal is used in order to synchronize the cameras among each other in post-processing. Live-monitoring of both the FT- and IMU sensor readings and a simulation of the robot were available at all times during the experiment, see figure 11. Only Linux devices were used in this framework.
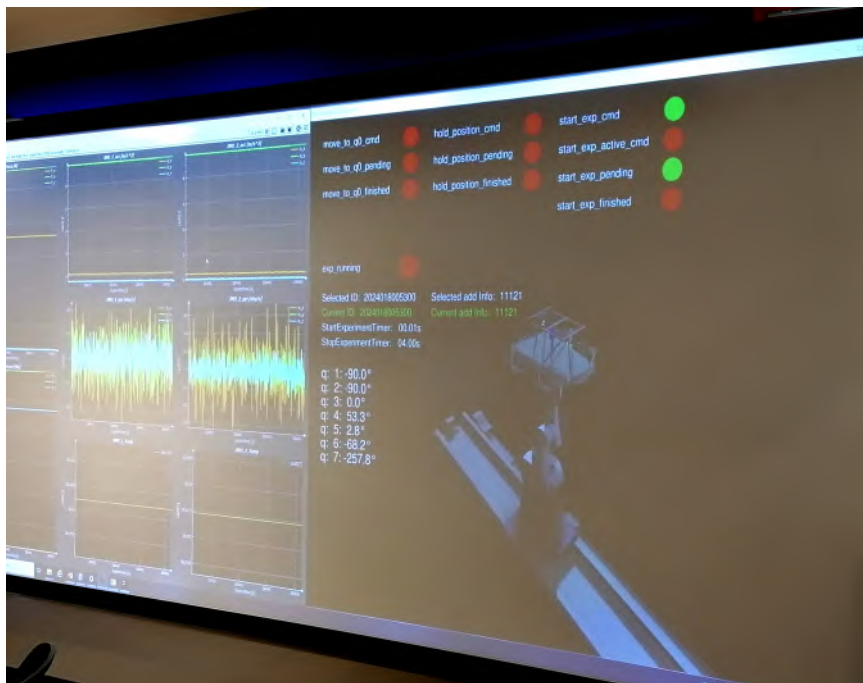

Figure 11 – Control room with live data of the sensors and a simulation of the current pose of the robot visualized with the DLR Visualization2 library [6].

Additional hardware for the control and support of the described sensors, such as circuit boards, power supply infrastructure and measurement amplifier of the FT sensor are also placed on the bottom side of the Aluminum base plate, as seen in figure 12.

4.5 Measurement Matrix

For the selection of the measurement matrix, several aspects had to be considered to cover a satisfactory number of sloshing scenarios for the purpose of validation of the CFD simulation for the given application.

- Inclusion of some generic cases to assure a correct fundamental system representation (comparatively low complexity of the flow problem)

- Inclusion of aspects of the flow problem which have proven difficult in simulation and which have potential to affect the macroscopic response significantly (i.e. flow through connector holes)
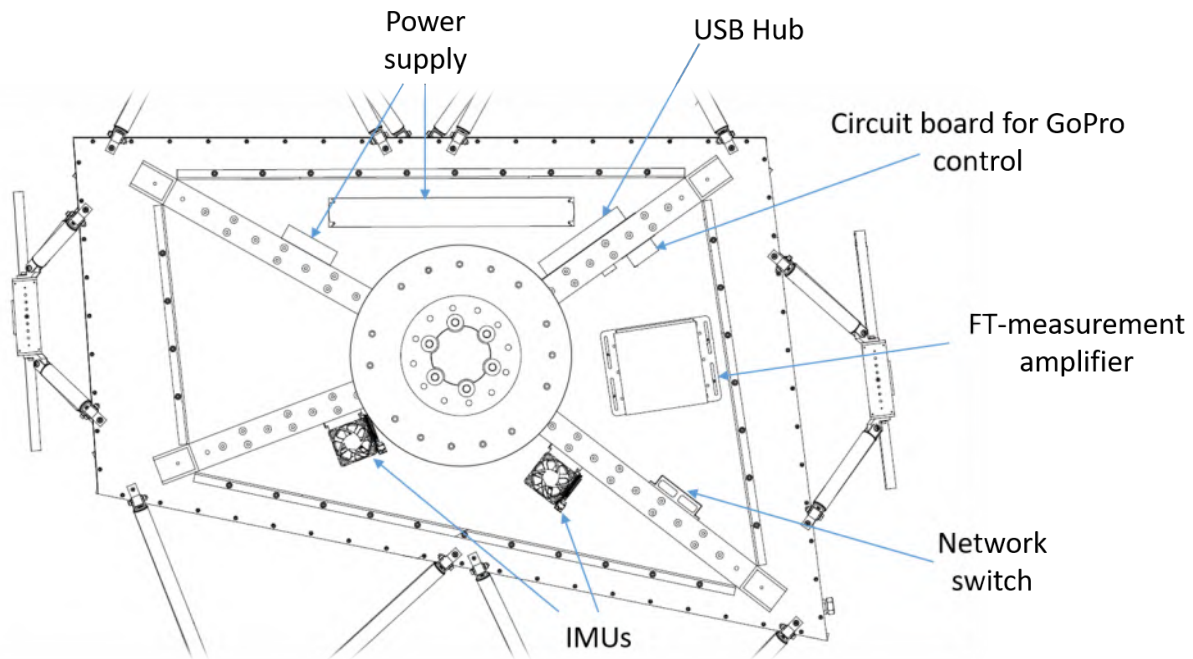
Figure 12 – Sensors placed on test bed bottom side.

- Inclusion of closer to reality scenarios that approach practical maneuvers relevant for a flight mechanic assessment of highly agile configurations.

As far as the maneuver selection is concerned, this resulted in three categories of maneuvers:

- Generic Pulse accelerations: Variation of the acceleration direction as well as the acceleration level and onset

- Generic periodic accelerations: Variation of acceleration direction as well as frequency / acceleration level

- Operationally relevant maneuvers: Selected based on typical application scenarios for the desired resulting ROM.

4.5.1 Implementation of maneuvers on the robotic motion platform

The generic types of maneuvers are intended to get a general idea of the behavior. Those maneuvers can be defined as elementary with simple movements along or around one Cartesian axis and combinations of them. Operationally relevant maneuvers mimic actual flight maneuvers in partly critical conditions. Those maneuvers have accelerations that are much higher than the used robot can provide, a scaling method is necessary, which is out of the scope of this paper. Details on that will be explained in a separate publication. The basic idea is to split the movement in high and low frequency parts to focus on the gradient of the acceleration while the low frequency parts are scaled down to be reproduced by the gravity. The basic thought here is that a constant, high acceleration without any change in direction will have a similar effect on the fluid as an acceleration with a smaller amplitude. The optimization procedure takes the accelerations of the maneuver as reference and optimizes for a set of joint angle trajectories (of all seven joints) that lead to a movement like the reference. In this global optimization approach with a sequential programming algorithm [8], all constraints of the system like joint angle limits, joint velocities limits and joint acceleration limits are taken into account. The outcome of that optimization is directly used to be replayed by the robot.

For the elementary tests there are two different types of movement: A pulse and a harmonic signal. The pulse is defined as a sudden movement along or around one Cartesian axis with a step in

acceleration followed by the exact opposite acceleration to reduce the velocity to zero. This acceleration profile is then reversed to end in the starting position, see figure 13. Here, some parameters define the profile like amplitude A, duration of acceleration t_{acc}, duration between acceleration and deceleration t_h and the pause between moving forward and backward t_p. For the harmonic signal, a sine function is used. Here, the parameters are the frequency f, amplitude A and the number of repetitions n.
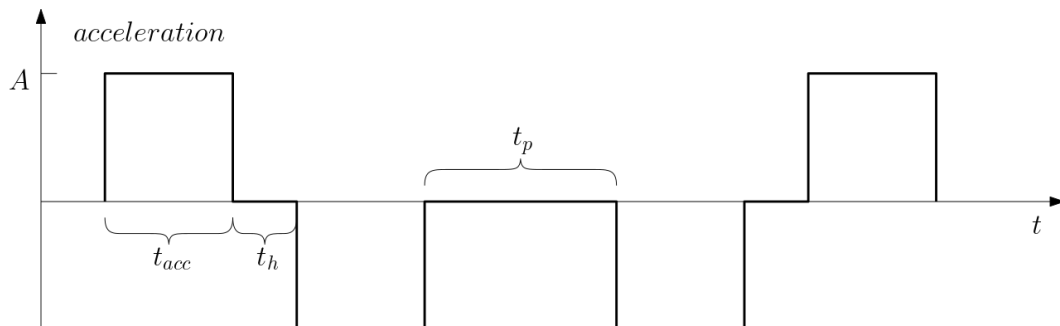

Figure 13 – Acceleration profile for a pulse movement.

In general, every trajectory was run twice to be able to assess the given repeatability. Figure 14 shows a capture of the execution of an operational maneuver.
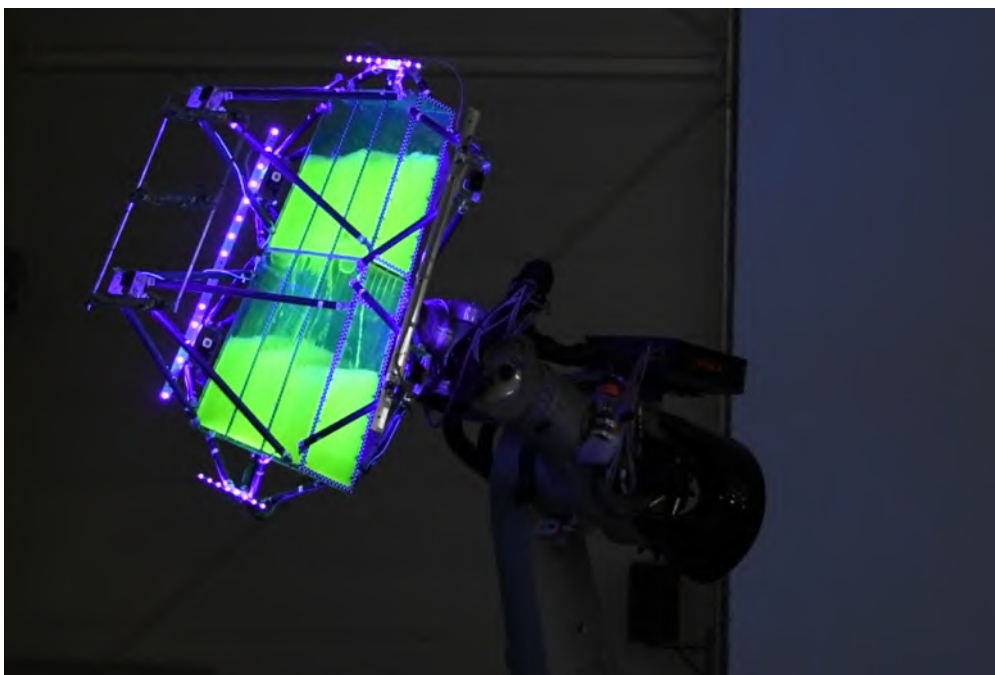

Figure 14 – Impression of the sloshing setup in operation.

4.5.2 Deducing Eigenfrequencies for periodic Maneuvers

As discussed in previous sections, providing sufficient experimental sloshing-data in the context of tool-validation for higher-order numerical codes (e.g. CFD, SPH) is essential for the success of these activities. Therefore, maximum pressure levels on the tank walls and thus large, highly non-linear fluid motions are of great interest. These flow-states usually occur around the first critical frequency (the respective Eigenfrequency of the confined fluid within its rigid compartment, e.g. figure 15). As exact computation is hard to achieve, a band-width needs to be determined, for which the nominal critical case can be safely assumed. The determination of these frequencies and respective consequences for each compartment are therefore described in this section.
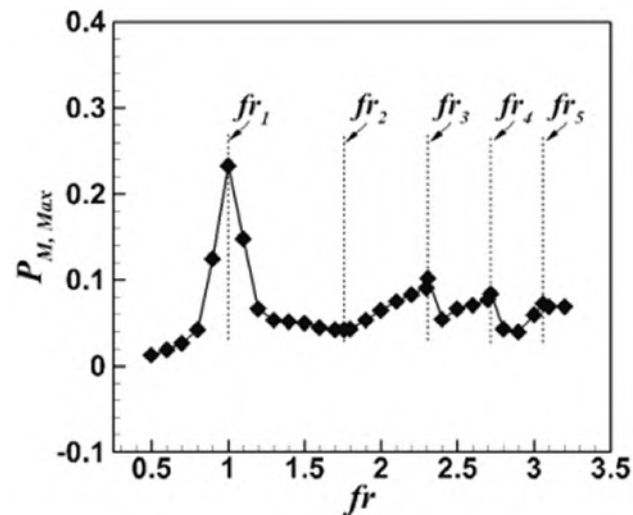
Figure 15 – Exemplary impact pressures P_M for a cuboid according to frequency ratios, with $fr = 1$ being the first Eigenfrequency, source [11] licensed under CC BY-NC-ND 4.0.

Three basic frequency ranges can be identified for each compartment and its respective fill-state:

- Excitation levels below the critical frequency result in fluid motion roughly synchronized with the rigid body motion - hence associated with the term **subcritical**

- The critical frequency value itself, causing a phase shift of 90 deg the fluid- vs. the rigid-motion - termed **critical**

- Cases above the critical frequency, causing only higher modes to be stimulated - the **supercritical** frequency range

Therefore, this separation is generally used as an important parameter for the "Measurement Matrix". Typically, two subcritical and one supercritical frequency has been selected for testing. These frequencies were selected in close vicinity (some 10-15% off) to the actual critical band-width, in order to provide a dynamic setup, and yet to stay away from potential resonance effects.

In order to determine feasible critical excitation frequencies for periodic maneuvers, the following process has been utilized:

1. Selection of a feasible analytical calculation scheme: The "Shallow Water Dispersion" formulation has been selected, as described in [11] and [13]

2. Approximation of the tank geometry (cuboid cells, wall length averaged) and individual fill state range for each compartment

3. Computation of longitudinal and lateral nominal critical frequencies, depending on the geometry and fill-state of each tank-compartment

4. Generation of a SPH setup (see [9], using the DualSPHysics code, see [10]) for one selected compartment (in our case C000, which is the largest single tank volume)

5. Deduction of the actual bandwidth of the critical frequency range around nominal values: A scaled frequency range from $fr = 0.7 \cdot f_c$ to $fr = 1.3 \cdot f_c$ in steps of $0.05 \cdot f_c$ was applied for SPH-analysis

6. Visual inspection of the derived solutions and application of the derived factors with the analytical results - resulting in an estimated bandwidth for the critical frequency

7. Selected excitation values for various fill-states - valid for all compartments - integrated with the Measurement Matrix

Utilizing the "Shallow Water Dispersion" formulation, the tank motion is assumed as pure surge (pure translation in the x- and y-directions), which follows a sinusoidal function given by:

$$x_T = A \cdot \sin(\omega_T t) \tag{3}$$

where A is the amplitude, ω_T the angular frequency, and x_T the translation.

The "Shallow Water Dispersion" formulation with ω_n as the n-th critical frequency can be derived for a rectangular cuboid with:

$$\omega_n = \sqrt{\frac{n\pi g}{L} \cdot \tanh\left(\frac{n\pi h}{L}\right)} \tag{4}$$

where L is the characteristic tank length, h is the fluid fill level, and n is the mode number.

The following assumptions and simplifications have been considered:

- Tank cells approximated as cuboids, with averaged dimensions in all axes

- No upper cell boundaries

- No damping effects

- No cross flows between compartments

As described above, a dedicated SPH setup has been created, in order to check potential scaling factors for the analytically derived nominal critical frequencies. The subsequent visual inspection (based on color-threshold for the particle speeds in figure 16) resulted in a sub-range from $fr = 0.8 \cdot f_c$ to $fr = 1.15 \cdot f_c$.

(a) Subcritical excitation ($fr = 0.7 \cdot f_c$)   (b) Critical excitation, nominal case ($fr = 1.0 \cdot f_c$)
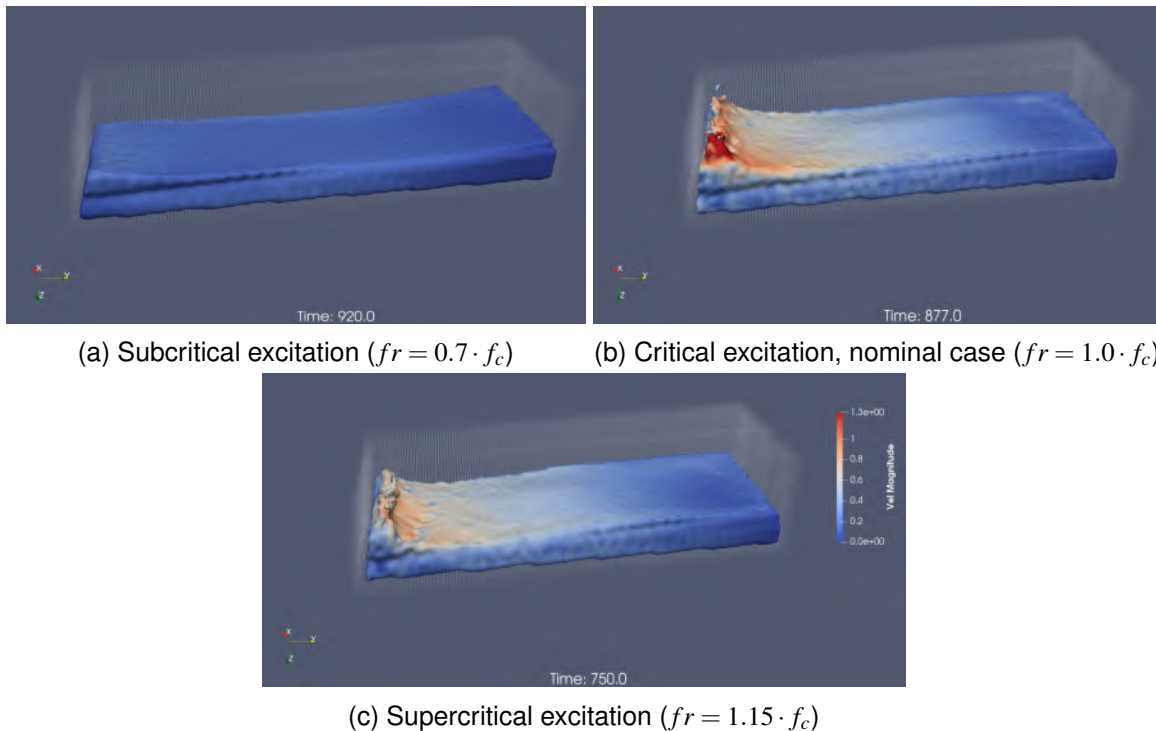
(c) Supercritical excitation ($fr = 1.15 \cdot f_c$)

Figure 16 – Impressions of the SPH-analysis for tank compartment C000.

Based on the analytical calculation and the subsequent adaptation to the SPH-derived factors, the critical frequencies for each compartment have been derived. Figure 17 shows the respective results, depending on the actual compartment geometry and fill-state (as measured for the highest compartment sidewall):
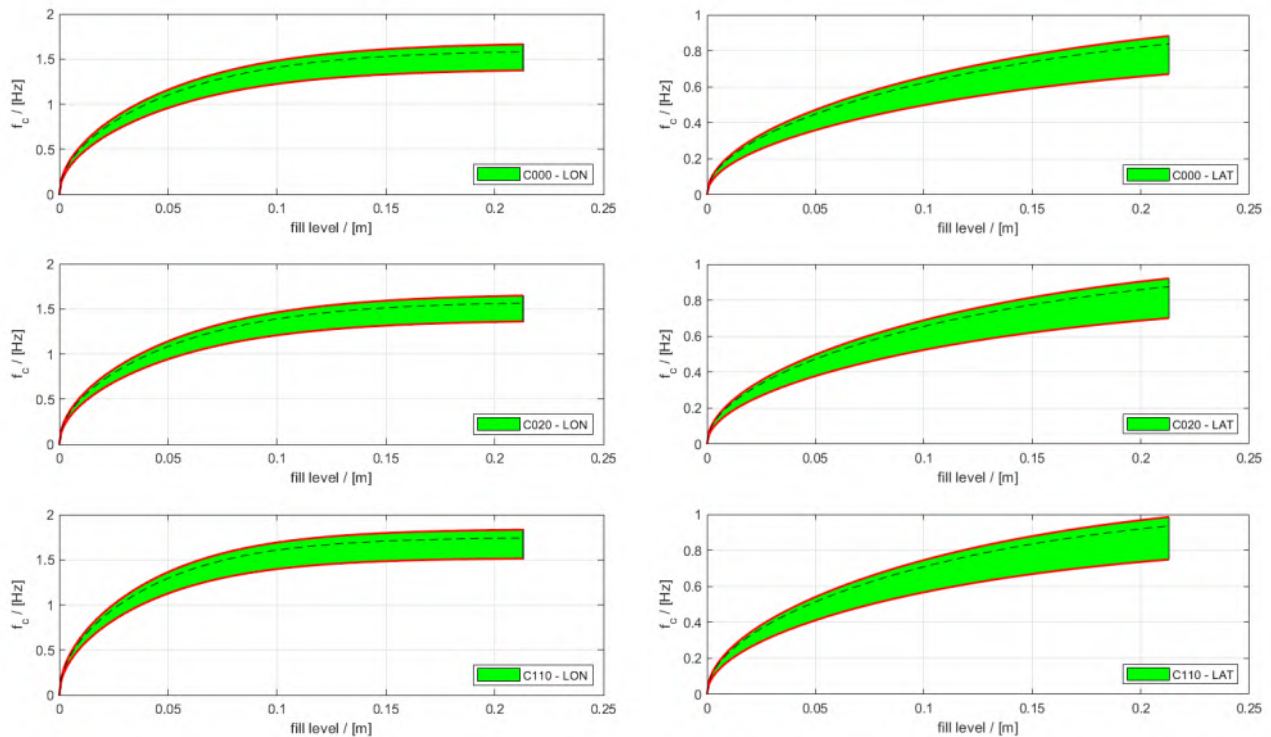
(a) Critical frequency range - Longitudinal motion   (b) Critical frequency range - Lateral motion

Figure 17 – Fill-State vs. Critical Frequencies for compartments C000, C020 and C110.

It is clearly visible, that a change in the characteristic dimension of the tank compartment directly leads to a change in the critical frequency. The results of this analysis have been integrated into the proposed frequencies of the Measurement Matrix. The deduced frequencies proved to be quite sufficient, when comparing the expected behavior with the respective experimental results.

4.5.3 Setup of the Measurement Matrix

The actual generation of the movement was not done in the Cartesian space because an inverse kinematics would have been necessary that is not trivial for over-actuated systems. Instead, an approach to generate the signals in the joint space was created, which was used for both types of elementary maneuvers.

As far as the starting orientation for the maneuvers is concerned, care was taken that it was chosen - depending on the respective fill level - such that each compartment would be filled to the same extent. Due to the skewed shape of the tank volume, this was necessary to avoid situations where flat compartments were completely filled while others were not for a horizontal orientation of the base plate.

Three different fill levels were investigated in the final measurement matrix, namely $35\,\%$, $50\,\%$ and $65\,\%$ of the tank volume.

As far as the variation in fluid and associated lighting conditions are concerned, a few different configurations were tested before launching the productive part of the measurement matrix. The fluid always consisted of distilled water with an additive of Ethylan 1003 as emulsifier (only $0.05\,\%$ in terms of volume). The surface tension was reduced to $30\,\mathrm{mN\,m^{-1}}$ through the usage of the latter. There were however the options with and without added Fluorescein-Natrium tested before deciding on just one productive combination for the measurement matrix. The final configuration along with the described camera settings was chosen to be the one including Fluorescein-Natrium as an additive.

A third variation that was included in the measurement matrix was the topology of the separator walls inside the tank. As mentioned before, the design was chosen such that the separator walls were interchangeable in a state there the tank was mounted to the robot flange. The choice to investigate different topologies of the primary cross-flow holes was motivated by the fact that initial investigations revealed difficulties in correctly representing the cross-flow with numerical simulations. One of the three different topologies of separator walls is schematically shown in figure 8. A second alternative features the primary cross-flow holes of circular shape. A third variation represents a scenario where the compartments are practically closed. The small holes at the top and bottom of the tank ensure a quasi-static compensation of the fluid level across the compartments to provide a deterministic initial condition for simulative reprediction. However, no significant cross-flow takes place during the performance of a trajectory. This last setup was added in order to further reduce the complexity in the case that difficulties in the match between test and simulation are found.

5. Data processing

For further usage in the process of CFD and SPH validation, the data gained in ground test undergoes a number of post-processing steps.

As mentioned before, synchronization between IMU and FT measurements is achieved through the usage of a NTP-server. Respective time-lags were identified consistently to add up to less than $5\,\mathrm{ms}$. Thus, this step does not have to be addressed further in post-processing. Both the IMU data and the FT data - each recorded with 1kHz sample frequency - are low-pass filtered with a cut-off frequency of 40Hz in order to remove noise in a first post-processing step.

The baseline for further post-processing steps is the transformation of all sensor data to a common reference point and test bed-fixed coordinate system. This is done based on the known installation angles with respect to a test bed-fixed system and position vectors with respect to the origin of the latter, as schematically sketched in figure 18.
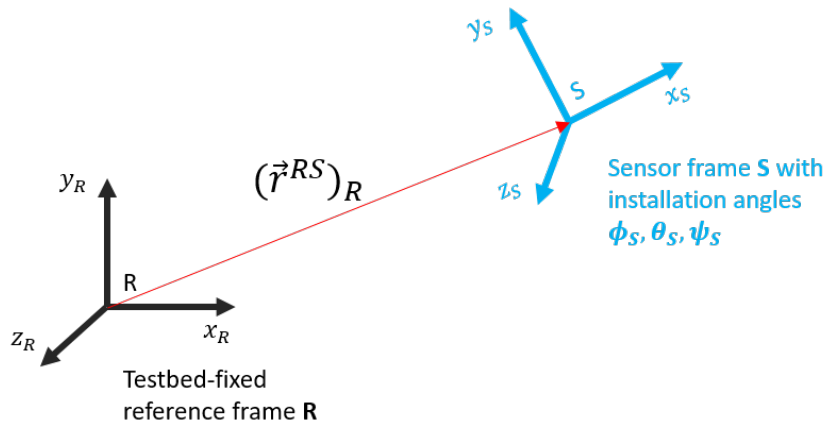

Figure 18 – Test bed-fixed and sensor frames.

The rotation matrix for transformation operations according to the definitions shown in figure 18 thus results in:

$$T_{RS} = \begin{bmatrix} cos\psi & sin\psi & 0 \\ -sin\psi & cos\psi & 0 \\ 0 & 0 & 1 \end{bmatrix} \begin{bmatrix} cos\theta & 0 & -sin\theta \\ 0 & 1 & 0 \\ sin\theta & 0 & cos\theta \end{bmatrix} \begin{bmatrix} 1 & 0 & 0 \\ 0 & cos\phi & sin\phi \\ 0 & -sin\phi & cos\phi \end{bmatrix} \tag{5}$$

As far as the IMU data are concerned, the following steps are performed in post-processing to provide all data relevant for further transformation operations as well as to deliver the necessary data as an input for recalculation operations:

- Filtering of the Raw Data

- Derivation of rotatory accelerations

- Transformation of translatory accelerations to the global reference point R

- Expression of translatory accelerations, rotatory speeds and rotatory accelerations in terms of the global reference frame R

The transformation of translatory accelerations is done assuming the test bed to be rigid as stated in equation 6 below:

$$\vec{a}^R = \vec{a}^S - \dot{\vec{\omega}}^{IR} \times \vec{r}^{RS} - \vec{\omega}^{IR} \times [\vec{\omega}^{IR} \times \vec{r}^{RS}] \tag{6}$$

In equation 6, $\vec{\omega}^{IR}$ denotes the rotatory speed of the tank with respect to the inertial frame.
To use the data gathered via the FT-sensor in comparison with CFD data, the following steps are run through:

- Filtering of the raw data

- Expression of the filtered forces and moments in terms of the global reference frame R

- Transformation of the measured moments to the global reference point R

- Deduction of the rigid body forces and moments at the reference point R to yield the sloshing forces and moments

The transformation of the measured moments to the global reference point R is also based on the assumption of a rigid body, simply accounting for the additional lever arm as derived from the known relative location of the FT sensor reference point to the global reference point.
The deduction of the rigid body forces and moments from the transformed measured results is crucial for comparison with CFD results. The latter yield the forces and moments that are exerted on the tank by the fluid. However, the installed sensor also measures any forces and moments induced by the rigid body motion of the empty tank mass. The latter must thus be deduced according to the rigid body motion equations 7 and 8:

$$m \cdot (\vec{a}^{dryCG})_R = (\vec{F})_R \tag{7}$$

$$m(\dot{\vec{M}}^{dryCG})_R = (I^{dryCG})_{RR} \cdot (\dot{\vec{\omega}}^{IB})_R \times [(I^{dryCG})_{RR} \cdot (\vec{\omega}^{IB})_R] \tag{8}$$

In equations 7 and 8, $dryCG$ denotes the center of gravity of the empty tank.
On top of the quantitative sources for comparison, also the GoPro data is post-processed for meaningful comparison with CFD visualizations. The following steps are performed:

- Synchronization of cameras among each other

- Synchronization of video material with other sensors

- Stacking of videos

- Introduce slow motion

- Down-sample videos

The synchronization of the cameras among each other is making use of a dedicated audio signal that was manually introduced during each test run. The audio trace is extracted and the videos are cut to match the same starting point according to the detected mismatch of the audio signal occurrence in each camera's audio stream. Care was taken to introduce a timely gap between the video "Start-up" signal and the "Switch-on" signal for the LED, such that the point in time where the LED are switched on is never cut-off from any video for synchronization purposes. The point in time where the LED are switched on can be associated with a global point in time thanks to its control via NTP. The associated timestamp is overlaid in each post-processed video for synchronization with the other sensors.
The videos are stacked with neighbouring cameras next to each other where possible. An example is shown in figure 19:

Figure 19 – Example of stacked post-processed camera recordings.

6. Summary and Outlook

The experimental setup was shown for a ground test with the aim to validate mid- and high-fidelity simulation methods of fuel sloshing for the application in highly agile aircraft tanks. Future work will include the re-calculation of the trajectories run in ground test for comparison with the gained experimental data, and thus validation of the aforementioned simulation methods. Validated simulation setups will further be used for tuning and development of reduced-order models related to fuel slosh.

7. Contact Author Email Address

lisa.debschuetz@airbus.com
richard.kuchar@dlr.de

8. Copyright Statement

The authors confirm that they, and/or their company or organization, hold copyright on all of the original material included in this paper. The authors also confirm that they have obtained permission, from the copyright holder of any third party material included in this paper, to publish it as part of their paper. The authors confirm that they give permission, or have obtained permission from the copyright holder of this paper, for the publication and distribution of this paper as part of the ICAS proceedings or as individual off-prints from the proceedings.

References

[1] Gambioli, F., Alegre Usach, R., Kirby, J., Wilson, T., Behruzi, P., Experimental Evaluation of Fuel Sloshing Effects on Wing Dynamics, International Forum on Aeroelasticity and Structural Dynamics (IFASD), 2019.

[2] Bellmann, T., Heindl, J., Hellerer, M., Kuchar, R., Sharma, K. & Hirzinger, G. The DLR Robot Motion Simulator Part I: Design and setup. *2011 IEEE International Conference On Robotics And Automation (ICRA)*. pp. 4694-4701 (2011)

[3] Bellmann, T., Seefried, A. & Thiele, B. The DLR Robots library - Using replaceable packages to simulate various serial robots. *Asian Modelica Conference 2020.*, 153-161 (2020), https://elib.dlr.de/138327/

[4] KUKA KUKA KR 360-3; KR 500-3 Specification. (KUKA Roboter GmbH, 2013, 9), Download at 10.05.2022 from https://www.kuka.com

[5] Bellmann, T. Optimierungsbasierte Bahnplanung für interaktive robotische Bewegungssimulatoren. (Universität der Bundeswehr München, 2014)

[6] Kümper, S., Hellerer, M. & Bellmann, T. DLR Visualization 2 Library - Real-Time Graphical Environments for Virtual Commissioning. *14th Modelica Conference*. pp. 197-204 (2021,9), https://elib.dlr.de/144780/

[7] Datasheet uIMU-M_IMU (Northrop Grumman LITEF GmbH), Download at 10.05.2022 from https://www.litef.de

[8] Pfeiffer, A. Optimization Library for Interactive Multi-Criteria Optimization Tasks. *9th International Modelica Conference*. pp. 669-679 (2012,9), https://elib.dlr.de/77222/

[9] Liu, M.B., and Liu, G.R., Smoothed particle hydrodynamics (SPH): an overview and recent developments., Archives of computational methods in engineering 17.1 (2010): 25-76.

[10] Domínguez JM, Fourtakas G, Altomare C, Canelas RB, Tafuni A, García-Feal O, Martínez-Estévez I, Mokos A, Vacondio R, Crespo AJC, Rogers BD, Stansby PK, Gómez-Gesteira M. 2021. DualSPHysics: from fluid dynamics to multiphysics problems. Computational Particle Mechanics. https://doi.org/10.1007/s40571-021-00404-2.

[11] Jae Hwan Jung, Hyun Sik Yoon & Chang Yeol Lee, Effect of natural frequency modes on sloshing phenomenon in a rectangular tank, International Journal of Naval Architecture and Ocean Engineering, Volume 7, Issue 3, 2015, Pages 580-594, https://doi.org/10.1515/ijnaoe-2015-0041.

[12] Akyildiz, H. & Unal, N.E., 2006. Sloshing in a three-dimensional rectangular tank: numerical simulation and experimental validation. Ocean Engineering, 33(16), pp.2135-2149., https://doi.org/10.1016/j.oceaneng.2005.11.001

[13] Armenio, V. & La Rocca, M. On the analysis of sloshing of water in rectangular containers: Numerical study and experimental validation. *1996 Ocean Engineering*, Volume 23, Issue 8, pp. 705-739, https://doi.org/10.1016/0029-8018(96)84409-X

[14] Zwart, S. D. *Scale Modelling in Engineering: Froude's Case.*. North-Holland, 2009.

[15] Bindczeck, B. *Konzeptionierung einer Versuchsplatform zur experimentellen Durchführung von Schwappversuchen*. Bachelor Thesis, FH Aachen, 2020.